Eur. J. Mineral., 33, 659–673, 2021
https://doi.org/10.5194/ejm-33-659-2021
© Author(s) 2021. This work is distributed under
the Creative Commons Attribution 4.0 License.

European Journal of Mineralogy
Open Access

Zinkgruvanite, $Ba_4Mn^{2+}_4Fe^{3+}_2(Si_2O_7)_2(SO_4)_2O_2(OH)_2$, a new ericssonite-group mineral from the Zinkgruvan Zn-Pb-Ag-Cu deposit, Askersund, Örebro County, Sweden

Fernando Cámara[1], Dan Holtstam[2], Nils Jansson[3], Erik Jonsson[4,5], Andreas Karlsson[2], Jörgen Langhof[2], Jaroslaw Majka[5,6], and Anders Zetterqvist[7]

[1]Dipartimento di Scienze della Terra "Ardito Desio", Università degli Studi di Milano, Via Luigi Mangiagalli 34, 20133, Milan, Italy
[2]Department of Geosciences, Swedish Museum of Natural History, Box 50007, 104 05 Stockholm, Sweden
[3]Department of Civil, Environmental and Natural Resources Engineering, Luleå University of Technology, 971 87 Luleå, Sweden
[4]Department of Mineral Resources, Geological Survey of Sweden, Villavägen 18, 752 36 Uppsala, Sweden
[5]Department of Earth Sciences, Uppsala University, Villavägen 16, 752 36 Uppsala, Sweden
[6]Faculty of Geology, Geophysics and Environmental Protection, AGH University of Science and Technology, al. Mickiewicza 30, 30-059 Kraków, Poland
[7]Zetterqvist Geokonsult AB, Kvarnbacksvägen 74, 168 74 Bromma, Sweden

Correspondence: Dan Holtstam (dan.holtstam@nrm.se)

Received: 2 July 2021 – Revised: 21 September 2021 – Accepted: 25 September 2021 – Published: 4 November 2021

Abstract. Zinkgruvanite, ideally $Ba_4Mn^{2+}_4Fe^{3+}_2(Si_2O_7)_2(SO_4)_2O_2(OH)_2$, is a new member of the ericssonite group, found in Ba-rich drill core samples from a sphalerite- and galena- and diopside-rich metatuffite succession from the Zinkgruvan mine, Örebro County, Sweden. Zinkgruvanite is associated with massive baryte, barytocalcite, diopside and minor witherite, cerchiaraite-Al, and sulfide minerals. It occurs as subhedral to euhedral flattened and elongated crystals up to 4 mm. It is almost black and semi-opaque with a dark-brown streak. The lustre is vitreous to sub-adamantine on crystal faces and resinous on fractures. The mineral is brittle with an uneven fracture. $VHN_{100} = 539$, and $H_{Mohs} \approx 4.5$. In thin fragments, it is reddish-black, translucent and optically biaxial (+), $2V_z > 70°$. Pleochroism is strong and deep brown-red ($\boldsymbol{E} \perp \{001\}$ cleavage) to olive-pale-brown. Chemical point analyses by WDS-EPMA (wavelength-dispersive X-ray spectroscopy electron probe microanalyser) together with iron valencies determined from Mössbauer spectroscopy yielded the empirical formula (based on 26 O+OH+F+Cl anions): $(Ba_{4.02}Na_{0.03})_{\Sigma 4.05}(Mn_{1.79}Fe^{2+}_{1.56}Fe^{3+}_{0.42}Mg_{0.14}Ca_{0.10}Ni_{0.01}Zn_{0.01})_{\Sigma 4.03}(Fe^{3+}_{1.74}Ti_{0.20}Al_{0.06})_{\Sigma 2.00}Si_4(S_{1.61}Si_{0.32}P_{0.07})_{\Sigma 1.99}O_{24}(OH_{1.63}Cl_{0.29}F_{0.08})_{\Sigma 2.00}$. The mineral is triclinic, in space group $P\bar{1}$, with unit-cell parameters $a = 5.3982(1)$ Å, $b = 7.0237(1)$ Å, $c = 14.8108(4)$ Å, $\alpha = 98.256(2)°$, $\beta = 93.379(2)°$, $\gamma = 89.985(2)°$ and $V = 554.75(2)$ Å^3 for $Z = 1$. The eight strongest X-ray powder diffraction lines are the following (d Å (I %; hkl)): 3.508 (70; 103), 2.980(70; $11\bar{4}$), 2.814 (68; $1\bar{2}2$), 2.777 (70; 121), 2.699 (714; 200), 2.680 (68; $20\bar{1}$), 2.125 (100; 124, 204) and 2.107 (96; $\bar{2}21$). The crystal structure ($R_1 = 0.0379$ for 3204 reflections) is an array of TS (titanium silicate) blocks alternating with intermediate blocks. The TS blocks consist of HOH sheets (H for heteropolyhedral and O for octahedral) parallel to (001). In the O sheet, the Mn^{2+}-dominant $M^O(1,2,3)$ sites give ideally Mn^{2+}_4 pfu (per formula unit). In the H sheet, the Fe^{3+}-dominant M^H sites and $A^P(1)$ sites give ideally $Fe^{3+}_2Ba_2$ pfu. In the intermediate block, SO_4 oxyanions and 11 coordinated Ba atoms give ideally $2\times$ SO_4Ba pfu. Zinkgruvanite is related to ericssonite and ferroericssonite in having the same topology and type of linkage of layers in the TS block. Zinkgruvanite is also closely compositionally related to yoshimuraite, $Ba_4Mn_4Ti_2(Si_2O_7)_2(PO_4)_2O_2(OH)_2$, via the coupled heterovalent substitution 2 Ti^{4+} + 2 $(PO_4)^{3-}$ → 2 Fe^{3+} +

2 $(SO_4)^{2-}$ but presents a different type of linkage. The new mineral probably formed during a late stage of regional metamorphism of a Ba-enriched, syngenetic protolith, involving locally generated oxidized fluids of high salinity.

1 Introduction

The ericssonite group of minerals (Sokolova et al., 2018) comprises two members: ericssonite, $BaMn_2Fe^{3+}(Si_2O_7)O(OH)$, and ferroericssonite, $BaFe^{2+}Fe^{3+}(Si_2O_7)O(OH)$, and two polytypes (orthorhombic and monoclinic, respectively). In both structures, an HOH block is the main structural unit, with Mn^{2+} and Fe^{2+} being the dominant cations in the O (octahedral) sheet of the HOH block (or TS block) and Fe^{3+} being the dominant cation at the [5]-coordinated sites along with Si_2O_7 groups of the H (heteropolyhedral) sheets. Ericssonite-group minerals have similar chemical properties (Ba sorosilicate) and are closely related to seidozerite-supergroup minerals (Sokolova and Cámara, 2017), which encompasses about 50 mineral species and polytypes, all characterized by TS (titanium silicate) blocks in the structural framework. Specifically, the ericssonite-group minerals are close to the bafertisite (with two Ti atoms per formula unit, apfu) and lamprophyllite (three Ti apfu) groups. The main difference in structure topology is the connection of octahedral and heteropolyhedral layers. Herein we describe a new mineral, zinkgruvanite, ideally $Ba_4Mn_4^{2+}Fe_2^{3+}(Si_2O_7)_2(SO_4)_2O_2(OH)_2$, which is a nominally Ti-free species closely related to yoshimuraite, $Ba_4Mn_4Ti_2(Si_2O_7)_2(PO_4)_2O_2(OH)_2$ (a bafertisite-group mineral) and innelite-1*A* $Ba_4(Na_2M^{2+}Ti)Ti_2(Si_2O_7)_2[(SO_4)(PO_4)]O_3(OH)$ (with M^{2+} = Mn, Fe^{2+}, Mg, Ca; a lamprophyllite-group mineral). The discovery of zinkgruvanite confirms the basis for a separate classification of the ericssonite-group minerals due to the bonding requirements of the $Fe^{3+}O_5$ polyhedron (cf. Sokolova and Cámara, 2014). The mineral association described here is unique, and members of the Ba-Cl-bearing cerchiaraite group (cf. Kampf et al., 2013) are also reported from Sweden for the first time.

The name of the mineral is given for the discovery locality, the Zinkgruvan mine, near Åmmeberg, municipality of Askersund, Örebro County, Sweden (58°49′ N, 15°6′ E; 170 m a.s.l.). The new mineral and mineral name have been approved by the Commission on New Minerals, Nomenclature and Classification, International Mineralogical Association (IMA2020-31). Type material (an incomplete drill core slice about 10 mm thick) is deposited in the type mineral collection of the Department of Geosciences, Swedish Museum of Natural History, Box 50007, 10405 Stockholm, Sweden, under catalogue number GEO-NRM 20170502.

2 Occurrence

The Palaeoproterozoic Zinkgruvan Zn-Pb-Ag-Cu deposit is a metamorphosed sulfide ore body which has been mined continuously since 1857, with nearby deposits worked at least as early as the 18th century (Tegengren, 1924; Haugard, 1944; Waldén, 1957). Stratiform sphalerite- and galena-dominated mineralization occurs here in a succession of interbedded metatuffite, marble and skarn (Hedström et al., 1989; Jansson et al., 2017). The host succession was deposited at ca. 1.89 Ga and overprinted by polyphase metamorphism and ductile deformation at ca. 1.87–1.86 and 1.84–1.80 Ga during the Svecokarelian orogeny (Stephens and Jansson, 2020). Peak metamorphic conditions are constrained to 750 ± 50 °C and 0.4–0.6 GPa in the area (Andersson et al., 1992; Gunn, 2002; Stephens et al., 2009). The stratiform sphalerite and galena mineralization has been heavily modified by deformation and metamorphism, including by recrystallization, by remobilization and locally by intrusion of partial melts formed by migmatization of pelitic rocks in the succession. Nevertheless, a syngenetic-exhalative origin has been suggested for the stratiform mineralization in most studies (Hedström et al., 1989; Allen et al., 1996; Jansson et al., 2017). Subordinate stratabound, dolomite-marble-hosted Cu-Zn mineralization occurs in the stratigraphic footwall in a vent-proximal position and is currently mined for Cu.

Zinkgruvanite was first noted by one of the authors (Nils Jansson) in two petrographic sections of drill core (from ca. 530 m depth) collected in conjunction with a research project (Jansson et al., 2017). The sampling was guided by earlier observations by Anders Zetterqvist, who had previously logged the core for Zinkgruvan Mining AB and noted an unusual Ba enrichment and an atypical mineral assemblage (Fig. 1). The core was drilled to explore the continuation of the stratiform Burkland Zn-Pb-Ag ore body at depth and intersects the mineralized zone at about the 1500 m level in the mine, in a proximal setting relative to an interpreted, fossil hydrothermal feeder zone (Jansson et al., 2017). The Ba-rich zone consists of massive baryte; radial, platy barytocalcite and minor witherite; cerchiaraite-Al; and sulfide minerals in a succession of sphalerite- and galena- and diopside-rich metatuffite and is in contact with a high-grade sphalerite- and galena-rich mineralization at both sides. This abundance of Ba is unusual for the deposit, in which Ba-bearing minerals are generally rare in the ore zone (Jansson et al., 2017).

Zinkgruvanite is found associated with barytocalcite, diopside, baryte, cerchiaraite-Al, cerchiaraite-Fe, witherite, galena, sphalerite, cubanite, chalcopyrite, pyrrhotite, pyrite

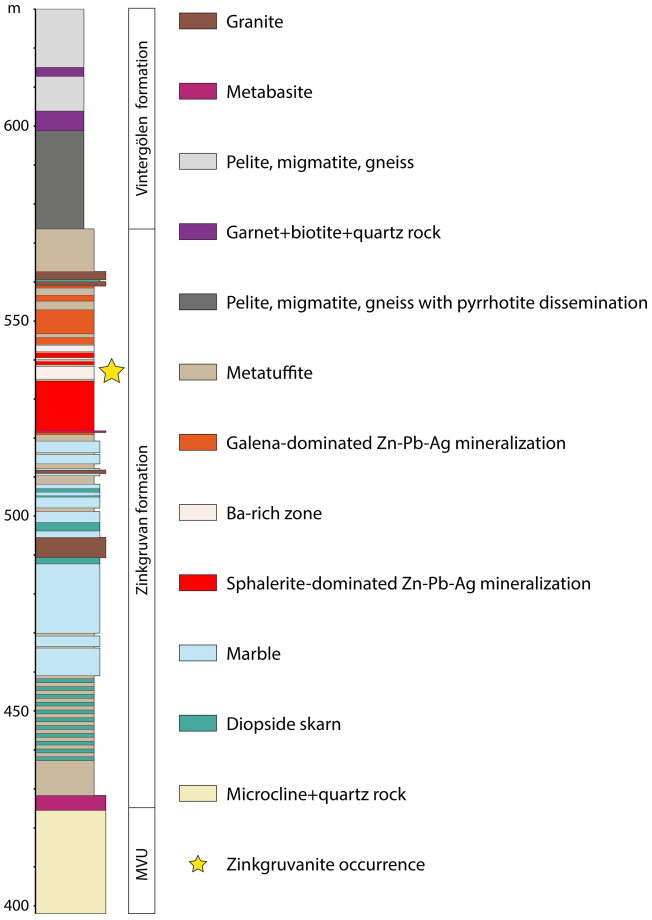

Figure 1. Drill core log section from the Zinkgruvan mine showing the position of the discovery location for the zinkgruvanite-bearing assemblage (yellow star). MVU: metavolcanic unit.

and zhangpeishanite. It locally occurs along grain boundaries of ferroan diopside crystals, partly intergrown with thin, elongated, locally parallel to sometimes fan-like aggregates of fibrous-to-acicular or fine-grained dustings of cerchiaraite-Al or in contact with sphalerite or as isolated euhedral-to-subhedral crystals and aggregates associated with baryte, barytocalcite and witherite (Fig. 2). Zinkgruvanite locally occurs overgrown by sulfides, specifically sphalerite. The cerchiaraite (sensu lato; s.l.) occurs in part as seemingly interstitial infillings between platy, parallel-to-radiating crystals of barytocalcite and baryte. Locally, textures suggest that cerchiaraite (s.l.) formed as a partial replacement of zinkgruvanite.

Two slightly different assemblages of zinkgruvanite have been observed in close vicinity to each other in the drill core. The first type is fine-grained and hosts quite abundant cerchiaraite (s.l.), both as very fine-grained masses and intergrowths or dustings and as discrete minute crystals, whereas the other type contains little or no cerchiaraite (s.l.) and is markedly coarser-grained.

Figure 2. Zinkgruvanite crystals in the type specimen. Field of view is 8 × 5 mm. Catalogue number GEO-NRM 20170502. Photo: Torbjörn Lorin.

3 Physical and optical properties

Zinkgruvanite occurs as subhedral-to-euhedral crystals up to 4 mm, with a platy habit, commonly flattened on {001} and elongated along [100], both as single crystals and in rare radiating aggregates. It is black, semi-opaque to reddish-black and translucent in thin fragments, with a dark-brown streak. The lustre is vitreous to sub-adamantine on crystal faces and resinous on fractures.

Zinkgruvanite shows perfect {001} and good {110} cleavages. The mineral is brittle with an uneven fracture. The density was not measured because of safety regulations concerning the heaviest liquids. A calculated value is 4.42(1) g/cm^3 based on the empirical formula and unit-cell volume obtained from single crystal XRD (X-ray diffraction) data. The hardness (Mohs) is estimated at 4–5 from scratch tests. Values obtained from micro-indentation (VHN_{100}) measurements, on a randomly oriented grain available in a polished section, using a Shimadzu M-type tester are 488–616 ($n = 10$, average 539), corresponding to ca. 4.5 Mohs. Pyramid indentations were straight to slightly convex; radial fractures were frequently observed, corresponding to the "star radial" and "simple shell" patterns, according to the terminology of Young and Millman (1964). The mineral is slowly soluble in 30 % HCl at room temperature, leaving a yellow solution and a white residue. Crystals are not attracted by a neodymium hand magnet.

Zinkgruvanite is transparent in thin section, with a biaxial (+) optical character, $2V_z > 70°$. The dispersion is strong, $r > v$. It exhibits a strong pleochroism in plane-polarized light, from deep brown-red ($\boldsymbol{E} \perp \{001\}$ cleavage) to olive-pale-brown (Fig. 3). Refractive indices were not determined directly, due to the strong absorption of the crystals and values close to the highest reference liquid available (1.80). The calculated overall n is 1.79 from Gladstone–Dale constants (Mandarino, 1981).

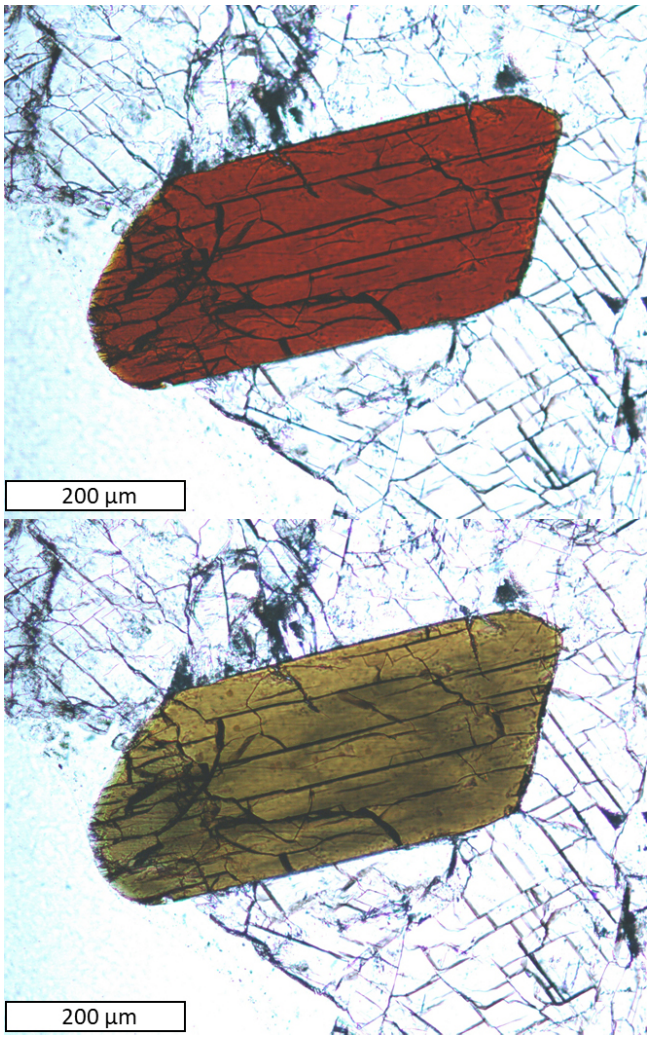

Figure 3. A zinkgruvanite crystal with baryte, barytocalcite and witherite. Thin section (30 µm), in transmitted polarized light, showing maximum pleochroism colours for 90° orientations.

4 Spectroscopic data

4.1 Reflectance

Polarized reflectance spectra were measured in air with an AVASPEC-ULS2048x16 spectrometer attached to a Zeiss Axiotron UV microscope (10x/0.20 Ultrafluar objective), using a halogen lamp (100 W) and a SiC (Zeiss no. 846) standard, with a circular measurement field ca. 100 µm in diameter. Results obtained in the 400–700 nm range (average of 600 scans, 100 ms integration time) are given in Table 1. The dispersion of the reflectance is normal, and the mineral is very weakly bireflectant.

Table 1. Reflectance values (%) measured in air (COM – Commission on Ore Mineralogy – wavelengths in italics).

λ (nm)	R_2	R_1	λ (nm)	R_2	R_1
400	8.74	8.53	560	7.97	7.77
420	8.46	8.25	580	7.87	7.67
440	8.41	8.20	*589*	7.87	7.68
460	8.25	8.03	600	7.86	7.69
470	8.21	8.07	620	7.74	7.67
480	8.12	7.96	640	7.81	7.68
500	8.05	7.86	*650*	7.80	7.65
520	7.97	7.82	660	7.74	7.65
540	7.92	7.78	680	7.76	7.64
546	7.98	7.79	700	7.79	7.65

4.2 Raman

A Raman spectrum of zinkgruvanite (Fig. 4) was collected from a randomly oriented crystal on a LabRAM HR 800 micro-spectrometer, using a 514 nm Ar-ion laser source at 1 mW power, a Peltier-cooled (−70 °C) CCD (charge-coupled device) detector (Synapse), an Olympus ULWD MS Plan 80x/0.75 na objective and a laser spot of 3 µm. Spectral positions were corrected against the Raman band at 464 cm^{-1} of pure quartz. The spectral resolution is about 1 cm^{-1}. Instrument control and data acquisition were made with the LabSpec 5 software. No laser-induced degradation of the mineral was observed. In the spectrum obtained, two bands related to O-H stretching vibrations of OH^- groups can be identified at 3655 and 3540 cm^{-1}. The strong band at 988 cm^{-1} is related to stretching vibration modes of the SO_4 groups, and the one at 887 cm^{-1} band is attributed to stretching of Si-O bonds. The band at 569 cm^{-1} and the strong band at 663 cm^{-1} are mainly due to O-Si-O bending vibrations. Overlapping of the latter band with a weak band of SO_4 bending vibrations having a close frequency is very likely (e.g. for IR band assignment; Chukanov and Chervonnyi, 2016). The weaker bands at lower wavenumbers (450 to 300 cm^{-1}) could be attributed to both (Mn,Fe)-O stretching modes and Si-O-Si bending vibrations, as well as resonance modes involving both kinds of vibrations, whereas bands at lowest frequencies are due to lattice vibrations.

4.3 Mössbauer

A ^{57}Fe transmission Mössbauer spectrum (Fig. 5) was obtained from a 5 mg powder absorber using a standard ^{57}Co(Rh) γ-radiation source (nominally 1.8 GBq). Two-mirror image spectra (±4.28 mm/s) were collected at 54.7° geometry to avoid texture effects, during 100 h over 1024 channels, and calibrated against an α-iron foil. The baseline of the resulting folded spectrum was at ca. 1.42×10^7 counts. Fitting and analysis were done with the MossA software (Prescher et al., 2012) assuming Lorentzian line shapes. An

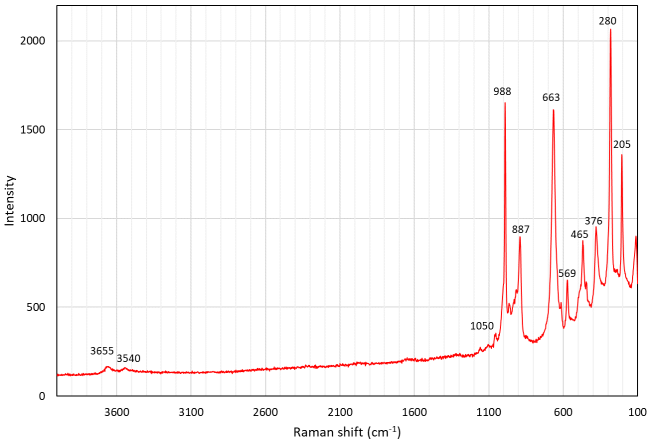

Figure 4. Raman spectrum of zinkgruvanite.

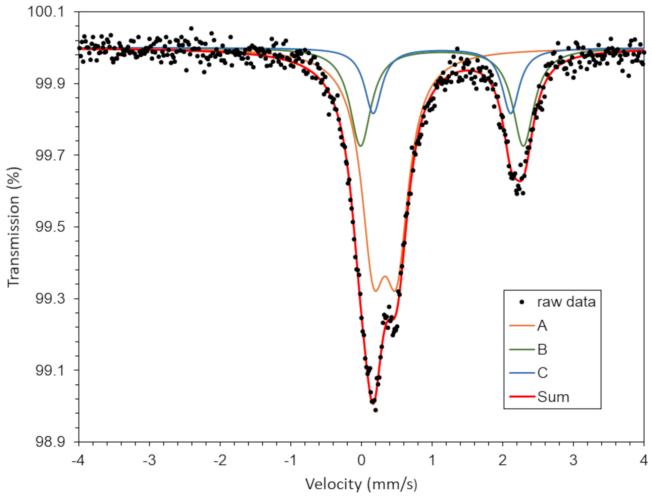

Figure 5. Mössbauer (^{57}Fe) spectrum of zinkgruvanite. See text for assignment of the three subspectra A, B and C.

absorption doublet (A; see Fig. 5) with centroid shift (CS) = 0.34(2) and quadrupole splitting (QS) = 0.32(2) mm/s is ascribed to Fe^{3+} in [5]-coordination by O, in analogy with data for ericssonite (Hålenius, 1995). Note that a minor contribution from [6]-coordinated Fe^{3+} that must be present according to structural data (see Sect. 7) is not well resolved in the spectrum. A pair of doublets (B and C in Fig. 5), constrained to have the same CS (= 1.14(2) mm/s), were used to fit the remaining absorption, with $QS_B = 2.30(10)$ and $QS_C = 1.95(10)$ mm/s, respectively. These values are consistent with Fe^{2+} (high spin) in [6]-coordination with O and very close to what was previously found in bafertisite-group minerals (Holtstam, 1998; Sokolova et al., 2009; Zhitova et al., 2017). Ideally, three doublets related to Fe^{2+}-enriched sites could be anticipated in the zinkgruvanite spectrum, but only two are distinguishable, probably due to the small differences in geometry of the corresponding coordination polyhedra. From area ratios, the fraction of Fe^{2+} is 42(10) % of total Fe. Full width at half maximum was in the range of 0.3–0.4 mm/s for the three doublets. The final χ^2 value was 0.8.

5 Chemical composition

The chemical composition was determined using an electron probe microanalyser (EPMA), a JXA-8530F JEOL Superprobe. Raw data were corrected using the PAP procedure (Pouchou and Pichoir, 1984). The instrument settings were 15 kV acceleration voltage, 10 nA beam current and 3 µm beam diameter. The number of point analyses was 30, collected from two grains. Reference materials, measured lines and analytical results are reported in Table 2. Strontium was below the detection limit in all point analyses. The H_2O concentration was not determined directly because of dearth of material. The presence of CO_2 is indicated neither by crystal structure refinement nor by spectroscopic data. Analytical data for selected associated Ba minerals are given in Table 3.

The empirical formula calculated on the basis of 26 anions (O+OH+F+Cl), accounting for known structural features (see below) and the iron valence determined from Mössbauer spectroscopy, is $(Ba_{4.02}Na_{0.03})_{\Sigma 4.05}(Mn_{1.79}Fe^{2+}_{1.56}Fe^{3+}_{0.42}Mg_{0.14}Ca_{0.10}Ni_{0.01}Zn_{0.01})_{\Sigma 4.03}(Fe^{3+}_{1.74}Ti_{0.20}Al_{0.06})_{\Sigma 2.00}Si_4(S_{1.61}Si_{0.32}P_{0.07})_{\Sigma 1.99}O_{24}(OH_{1.63}Cl_{0.29}F_{0.08})_{\Sigma 2.00}$ for crystal no. 1 (Table 2). The simplified formula is $Ba_4(Mn,Fe^{2+})_4(Fe^{3+},Ti)_2(Si_2O_7)_2[(S,Si,P)O_4]_2O_2(OH,Cl)_2$, and the ideal formula is $Ba_4Mn^{2+}_4Fe^{3+}_2(Si_2O_7)_2(SO_4)_2O_2(OH)_2$, which requires BaO 41.58, MnO 19.23, Fe_2O_3 10.83, SiO_2 16.29, SO_3 10.85 and H_2O 1.22 for a total 100 wt %. Although this formula could be reduced by a factor of 2, it is kept in this way, with $Z = 1$, to emphasize the close relation to the seidozerite-supergroup minerals.

6 X-ray crystallography

Powder X-ray diffraction data were collected with a Panalytical X'Pert^3 powder diffractometer equipped with an X'Celerator silicon-strip detector and operated at 40 mA and 45 kV (Cu $K\alpha$ radiation, $\lambda = 1.5406$ Å). Bragg peak positions (Table 4) were determined with the Panalytical HighScore Plus 4.6 software and corrected against an external Si standard (NBS 640b; National Bureau of Standards). The triclinic ($P\bar{1}$) unit-cell parameters refined by the least-squares method from the powder data are $a = 5.3989(6)$ Å, $b = 7.0319(8)$ Å, $c = 14.821(2)$ Å, $\alpha = 98.274(11)°$, $\beta = 93.436(12)°$, $\gamma = 90.087(10)°$ and $V = 555.77(9)$ Å^3 for $Z = 1$.

A single-crystal X-ray study was done on a crystal fragment (0.050 × 0.125 × 0.190 mm) with a Rigaku XtaLAB Synergy with a hybrid pixel array detector, with graphite-monochromatized Mo$K\alpha$ radiation ($\lambda = 0.71073$ Å); work-

Table 2. Chemical data (in wt %) for zinkgruvanite.

Constituent	Crystal no. 1 $n = 15$		Crystal no. 2 $n = 15$		EPMA reference material
	Mean	2σ	Mean	2σ	
SiO_2	17.38	0.34	17.47	0.32	($K\alpha$, TAP) – wollastonite
TiO_2	1.05	0.12	1.21	0.25	($K\alpha$, PET) – pyrophanite
Al_2O_3	0.20	0.06	0.22	0.07	($K\alpha$, TAP) – Al_2O_3
Cr_2O_3	0.01	0.04	0.01	0.04	($K\alpha$, LIF) – Cr_2O_3
[FeO]	17.94	0.44	18.36	0.47	($K\alpha$, LIF) – fayalite
FeO[a]	7.53		7.71		
Fe_2O_3[a]	11.56		11.84		
MnO	8.49	0.32	7.70	0.27	($K\alpha$, LIF) – pyrophanite
ZnO	0.03	0.08	0.04	0.08	($K\alpha$, LIF) – ZnO
NiO	0.03	0.06	0.02	0.07	($K\alpha$, LIF) – NiO
V_2O_5	0.03	0.06	0.03	0.04	($K\alpha$, LIF) – vanadinite
P_2O_5	0.31	0.28	0.96	0.70	($K\alpha$, PET) – apatite
MgO	0.37	0.06	0.38	0.07	($K\alpha$, TAP) – MgO
CaO	0.39	0.06	0.36	0.12	($K\alpha$, PET) – wollastonite
Na_2O	0.07	0.08	0.06	0.10	($K\alpha$, TAP) – albite
K_2O	0.01	0.02	0.01	0.02	($K\alpha$, PET) – orthoclase
BaO	41.26	0.36	41.29	0.40	(Lα, PET) – baryte
F	0.10	0.16	0.04	0.14	($K\alpha$, LDE1) – apatite
Cl	0.70	0.06	0.60	0.12	($K\alpha$, PET) – apatite
SO_3	8.63	0.32	8.00	0.92	($K\alpha$, PET) – baryte
H_2O[b]	0.99		1.01		
$O \equiv Cl, F$	−0.20		−0.17		
Total	98.93		98.79		

[a] Based on Mössbauer spectroscopy. [b] Calculated from structure (OH+F+Cl) = 2.

ing conditions were 50 kV and 1 mA, and the detector-to-sample distance was 6.2 cm. A combination of ω and ϕ scans, with a step scan of 0.5° and exposure time of 2 s per frame were used to maximize redundancy and data coverage.

The crystal structure was solved by direct methods and refined to $R1 = 0.032$ in SHELXTL (Sheldrick, 2015) using neutral-atom scattering curves from the *International Tables* (Wilson, 1992). Experimental details, unit-cell parameters and R indices are given in Table 5. Fractional atom coordinates, site occupancies and isotropic-displacement parameters are reported in Table 6. Bond distances are given in Table 7. A crystallographic information file (CIF) containing observed structure factors has been deposited as the Supplement.

The crystal structure of zinkgruvanite contains an HOH layer (see Sokolova and Cámara, 2017, for nomenclature) as the main structural unit (Fig. 6a). The dominant cations in the central O (octahedral) sheet of the HOH layer are Mn^{2+} and Fe^{2+}; they are distributed over three octahedral sites ($M(1)$, $M(2)$ and $M(3)$); the two adjacent H sheets are composed of [5]-coordinated Fe^{3+} polyhedra M^{H} and Si_2O_7 groups ($Si(1)$ and $Si(2)$ sites). Between the HOH layers, there is a distorted layer of Ba atoms at two cation sites, $A^P(1)$ and B^P, on the periphery of the HOH layer, and a TS block. The $A^P(1)$ and B^P sites coordinate (SO_4) and configure the I block (intermediate block, in the sense of Sokolova, 2006). At convergence, a split model was applied to the A^P and X_A^O sites. The latter was interpreted as resulting from partial occupancy by Cl in agreement with the chemical analysis (Table 2). It was not possible to locate the position of H atoms in the difference Fourier maps, probably due to the split site related to Cl.

7 Discussion

7.1 Crystal structure and crystal chemistry

7.1.1 Cation sites

In the heteropolyhedral sheet, tetrahedral sites are occupied solely by Si in zinkgruvanite, as confirmed by the average observed bond lengths (1.620–1.624 Å, Table 7). The M^{H} sites are dominantly occupied by Fe^{3+} with minor Ti and Al ($Ti_{0.20}Al_{0.06}$), and the observed average bond length is 1.964 Å, larger than that in yoshimuraite (1.923 Å), where it is dominantly occupied by Ti (0.78 apfu), and minor Fe^{3+} (0.22 apfu) (McDonald et al., 2000). The calculated site scat-

Table 3. Composition (in wt %) of barium-bearing minerals associated with zinkgruvanite.

	Cerchiaraite-Al $n = 10$		Barytocalcite $n = 11$		Witherite $n = 8$	
	Mean	σ	Mean	σ	Mean	σ
SiO_2	25.34	0.38	–	–	–	–
TiO_2	0.61	0.06	–	–	–	–
Al_2O_3	10.23	0.68	–	–	–	–
V_2O_3	0.01	0.02	–	–	–	–
Cr_2O_3	0.02	0.03	–	–	–	–
MgO	0.10	0.05	–	–	–	–
CaO	0.05	0.02	19.06	0.17	0.69	0.07
BaO	44.27	0.77	50.40	0.46	76.68	0.59
SrO	–	–	0.18	0.17	0.58	0.16
Fe_2O_3	6.85	0.82	0.03	0.03	0.04	0.05
MnO	0.71	0.10	–	–	–	–
NiO	0.01	0.01	–	–	–	–
Na_2O	0.12	0.06	–	–	–	–
K_2O	0.00	0.00	–	–	–	–
Cl	6.52	0.12	–	–	–	–
SO_3	0.01	0.02	–	–	–	–
CO_{2calc}			29.60		22.30	
H_2O_{calc}	4.90					
$O \equiv Cl$	−1.47					
Total	98.29		99.27		100.29	

Table 4. Powder X-ray diffraction data (d in Å) for zinkgruvanite.

I	I_{calc}	d_{obs}	d_{calc}	h	k	l
53	47	4.875	4.880	0	0	3
32	32	4.231	4.228	1	1	$\bar{1}$
26	47	4.163	4.155	1	$\bar{1}$	1
30	47	3.908	3.906	1	1	$\bar{2}$
35	32	3.730	3.732	1	0	$\bar{3}$
42	78	3.632	3.632	$\bar{1}$	1	2
70	44	3.508	3.512	1	0	3
	48		3.497	0	2	$\bar{1}$
51	21	3.445	3.440	1	1	$\bar{3}$
56	83	3.330	3.334	0	2	$\bar{2}$
48	68	3.154	3.156	$\bar{1}$	1	3
56	40	3.108	3.117	1	0	$\bar{4}$
70	70	2.9799	2.9775	1	1	$\bar{4}$
61	35	2.9275	2.9298	1	$\bar{2}$	1
61	60	2.8401	2.8394	1	$\bar{1}$	4
68	75	2.8136	2.8130	1	$\bar{2}$	2
70	92	2.7771	2.7733	1	2	1
71	43	2.6990	2.6945	2	0	0
85	74	2.6804	2.6791	2	0	$\bar{1}$
40	20	2.5782	2.5799	2	0	$\bar{2}$
16	11	2.4782	2.4802	2	0	2
15	13	2.4200	2.4187	0	2	$\bar{5}$
45	32	2.2365	2.2357	2	0	$\bar{4}$
25	28	2.2090	2.2053	0	1	6
31	26	2.1709	2.1719	1	$\bar{2}$	5
	27		2.1271	2	$\bar{2}$	1
100	26	2.1250	2.1242	1	2	4
	17		2.1095	2	0	4
96	21	2.1071	2.1063	$\bar{2}$	2	1
58	17	2.0755	2.0776	2	$\bar{2}$	2
32	18	1.9876	1.9872	$\bar{1}$	2	5
21	15	1.8403	1.8426	0	3	4
49	40	1.7570	1.7574	0	4	$\bar{1}$
29	10	1.6537	1.6540	$\bar{3}$	1	3
42	9	1.5926	1.5933	3	2	$\bar{2}$
29	11	1.4695	1.4683	2	$\bar{4}$	0

tering values agree well with the site scattering obtained by structure refinement (Table 8).

There are four M^O [6]-coordinated sites in the O sheet: $M(1)$, two $M(2)$ and $M(3)$. These are occupied dominantly by Mn^{2+}, although Fe^{2+} is also very abundant. The $M(1)$ and $M(2)$ polyhedra are slightly smaller (and probably host minor Fe^{3+}), whereas the $M(3)$ polyhedron is larger, and we assume that it hosts some Ca, which is coupled to the replacement of (OH) by Cl at the X_A^O site. The same trend in polyhedron size occurs in yoshimuraite ($M(1) \approx M(2) < M(3)$; McDonald et al., 2000), with larger average bond distances because of the higher Mn^{2+} content. Average bond distances in zinkgruvanite (Table 7) and the observed bond valence sums (Table 6) agree with dominance of Mn^{2+} at the M^O sites. Agreement between aggregated observed site scattering and calculated site scattering from the assigned site population is close (97.2 vs. 100.1 epfu; electrons per formula unit).

There are two types of peripheral sites: the A^P sites that are closer to the TS block and the B^P sites, which are part of the intermediate layer along with oxyanions (in this case the SO_4 groups). The A^P sites are split into two sites: $A^P(1)$ (occupied by Ba, 1 apfu) and $A^P(2)$, a satellite peak due to minor Na (0.03 apfu; Table 1) being bonded to F at the X_A^O anion site (0.08 apfu) close to the O sheet, whereas Ba at the $A^P(1)$ is further from the O sheet to avoid steric hindrance with the H associated with OH at the X_A^O anion site ($A^P(1)$–$X_A^O = 3.57$ Å). This could explain the rather short stretching frequencies for (OH^-) in the Raman spectrum (3655 and 3540 cm^{-1}). The presence of two different Raman shifts must be ascribed to the dominant Mn^{2+} and Fe^{2+} at the two $M(2)$ and the $M(1)$ sites, i.e. Mn^{2+} and Fe^{2+}. Mean bond lengths are compatible with Ba at the $A^P(1)$ site, and Na is at the $A^P(2)$ site (coordinating Cl at X_A^O). The B^P site is fully occupied by Ba, as shown by the observed site scattering and mean bond lengths (Table 6).

In the intermediate block, Ba and SO_4 form a baryte-like layer parallel to (010) (Fig. 7a and b). The overall geometry is the same as in baryte, although some distortion is present to adapt to bonding to the oxygens of the Si_2O_7 and $Fe^{3+}O_5$ groups of the H sheet. The S-S distances in the intermediate block of zinkgruvanite are 4.015 and 5.313 Å, whereas the

Table 5. Crystal data and experimental conditions for the single-crystal XRD study.

Temperature	293(2) K
Wavelength	0.71073 Å
Crystal system	Triclinic
Space group	$P\bar{1}$
Unit-cell dimensions	$a = 5.39820(10)$ Å, $\alpha = 98.256(2)°$.
	$b = 7.02370(10)$ Å, $\beta = 93.379(2)°$.
	$c = 14.8108(4)$ Å, $\gamma = 89.985(2)°$.
Unit-cell volume	554.75(2) Å^3
Z	1
Absorption coefficient	11.140 mm^{-1}
$F(000)$	666
Theta range for data collection	3.78 to 30.03°.
Index ranges	$-7 \leq h \leq 7$, $-9 \leq k \leq 9$, $-20 \leq l \leq 20$
Reflections collected	14 768
Independent reflections	3204 ($R_{\rm int} = 0.0499$)
Completeness to $\theta = 30.03°$	98.5 %
Refinement method	Full-matrix least-squares on F^2
Data/restraints/parameters	3204/0/209
Goodness of fit on F^2	1.030
Final R indices [$I > 2\sigma(I)$]	$R1 = 0.0323$, w$R^2 = 0.0758$
R indices (all data)	$R1 = 0.0379$, w$R^2 = 0.0787$
Largest diff. peak and hole	1.751 and −1.361 e.Å^{-3}

corresponding values for baryte are 4.002 and 5.000 Å (using the atom coordinates of Jacobsen et al., 1998). The mean S-O bond length is 1.471 Å, which agrees well with a site dominantly occupied by S. A similar average bond length was reported for yoshimuraite (1.487 Å) by McDonald et al. (2000) for an S-site occupancy of $(P_{0.46}S_{0.34}Si_{0.17})_{\Sigma 0.97}$ and an incident bond valence of 5.5 v.u. (Table 5 of McDonald et al., 2000; valence unit). Incident bond valence calculated with full occupancy yields values too high at O(6) and O(7) but good values for O(1) and O(13) that show bond valence deficiency.

7.1.2 Anion sites

There are 13 anion sites in the structure of zinkgruvanite, 12 of which are fully occupied by O^{2-}, as indicated by the incident bond valence (Table 6). The $X_A^{\rm O}$ bonds to two $M(2)$ and one $M(3)$ cations, and its incident bond valence (Table 6) indicates that $X_A^{\rm O}$ must host a monovalent anion, dominantly (OH^-) substituted by minor F or Cl. The O(13) site bonds to the cations at the S and B^P sites and shows a prominent bond valence deficiency and high $U_{\rm eq}$ (Table 6 and Fig. 6a) that is related to the heterovalent substitutions at the S sites (S^{6+} substituted by P^{5+} and Si^{4+}). The O(1) site also shows a high equivalent isotropic-displacement factor (Table 6) and is also bonded to cations at the S, B^P and A^P sites. Also in this case, the high displacement parameters are likely due to static disorder to be ascribed to heterovalent substitutions at the S site. Bond valence has been calculated assuming an occupancy of 0.87 S atoms per site. Full occupancy by S increases incident bond valence at O(1) and O(13) to values closer to 2 v.u., but values at O(6) and O(7) become too high (2.14 and 2.12 v.u., respectively). This indicates that full occupancy of the S site by sulfur requires smaller cations at A^P and B^P. Therefore, heterovalent substitution of S by P (or Si) is favoured.

7.1.3 Nomenclature and classification

Zinkgruvanite is a member of the ericssonite group and is strongly related to ericssonite and ferroericssonite by the insertion of SO_4 groups at the I block and by the substitutions of Mn^{2+} by Fe^{2+} at the O sheet in ferroericssonite. It is closely related to the minerals of the seidozerite supergroup, specifically to yoshimuraite, $Ba_4Mn_4Ti_2(Si_2O_7)_2(PO_4)_2O_2(OH)_2$, via the coupled heterovalent substitution 2 Ti^{4+} + 2 $(PO_4)^{3-} \rightarrow$ 2 Fe^{3+} + 2 $(SO_4)^{2-}$, and innelite-1A, $Ba_4Ti_2(Na_2M^{2+}Ti)(Si_2O_7)_2[(SO_4)(PO_4)]O_2[O(OH)]$, via the additional coupled heterovalent substitution $(SO_4)^{2-} + {}^{M^{\rm O}}(Na_2Ti)^{6+} + {}^{X_A^{\rm O}}O^{2-} \rightarrow (PO_4)^{3-} + {}^{M^{\rm O}}(Mn_3^{2+})^{6+} + {}^{X_A^{\rm O}}OH^-$.

In yoshimuraite there is a topological change accompanying this substitution, as discussed by Sokolova and Cámara (2014), that it is related to the linkage of H sheets to the O sheet in the TS block. The differences in linkage in the TS block between these two minerals are clearly visible in Fig. 6. The HOH layer in which the $M^{\rm H}$ sites are occupied by $Fe^{3+} = 2$ apfu (Fig. 6a, zinkgruvanite, and Fig. 8, ferroericssonite) has linkage 1 (in the sense of Sokolova, 2006): two

Table 6. Atom coordinates and equivalent isotropic displacement parameters (Å^2) for zinkgruvanite. U_{eq} is defined as one-third of the trace of the orthogonalized U^{ij} tensor.

Site and ref. s.c.*	x	y	z	U_{eq}	s.o.f.	B.V.
B^P Ba	1.23102(5)	1.12167(4)	0.883149(19)	0.01622(11)	0.989(4)	2.253
$A^P(1)$ Ba	0.71960(6)	0.58658(4)	0.81206(4)	0.01783(15)	0.985(5)	2.061
$A^P(2)$ Ba	0.721(4)	0.569(3)	0.770(3)	0.021	0.016(2)	0.033
M^H Fe	−0.29776(12)	0.05864(9)	0.69843(5)	0.0119(2)	0.983(5)	2.862
$M(1)$ Fe	0	1/2	1/2	0.0130(3)	0.483(3)	2.102
$M(2)$ Fe	0.49965(13)	0.76557(11)	0.50054(5)	0.0161(3)	0.922(3)	1.961
$M(3)$ Fe	0	1/2	1/2	0.0159(4)	0.466(3)	2.048
$Si(1)$ Si	0.1992(2)	0.78356(16)	0.68739(8)	0.0101(3)	1	4.001
$Si(2)$ Si	0.1984(2)	0.32982(16)	0.68489(8)	0.0102(3)	1	4.043
S	1.2468(3)	0.6968(2)	0.97635(10)	0.0187(5)	0.874(8)	5.250
O(1)	1.2639(8)	0.7150(7)	1.0777(3)	0.0323(10)	1	1.850
O(2)	−0.0383(6)	0.2617(5)	0.7335(2)	0.0144(7)	1	2.035
O(3)	0.4541(6)	0.8791(5)	0.7362(2)	0.0155(7)	1	1.970
O(4)	−0.0395(6)	0.8792(5)	0.7368(2)	0.0148(7)	1	1.978
O(5)	0.4531(6)	0.2615(5)	0.7327(2)	0.0157(7)	1	2.019
O(6)	1.4635(7)	0.7978(6)	0.9483(3)	0.0256(8)	1	1.946
O(7)	1.0199(7)	0.7983(6)	0.9488(3)	0.0254(8)	1	1.932
O(8)	0.1782(6)	0.2737(5)	0.5749(2)	0.0153(7)	1	2.002
O(9)	−0.3156(6)	0.0204(5)	0.5721(2)	0.0150(7)	1	1.980
O(10)	0.2025(7)	0.5643(5)	0.7135(3)	0.0209(8)	1	2.046
$X^O_{A(OH)}$	0.327(2)	0.4823(18)	0.4322(7)	0.0236(16)	0.77(1)	0.760
$X^O_{A(Cl)}$	0.324(3)	0.469(2)	0.4018(7)	0.0236(16)	0.23(1)	0.303
O(12)	0.1796(6)	0.7766(5)	0.5773(2)	0.0149(7)	1	1.942
O(13)	1.2390(11)	0.5045(7)	0.9278(5)	0.0474(16)	0.874(8)	1.761

* ref. s.c.: scattering curve used for refine site occupancy. s.o.f.: site occupancy factor. B.V.: bond valence calculated with values from Gagné and Hawthorne (2015), except for bonds involving Cl taken from Brown and Altermatt (1985), and the ideal chemical composition (except for S site at 0.87 apfu of S; see text for discussion).

Si_2O_7 groups of two H sheets link to the trans edges of an octahedron of the O sheet in zinkgruvanite and ferroericssonite (Fig. 9f). Where the M^H sites are occupied by $Ti^{4+} = 2$ apfu, as in yoshimuraite (Fig. 6b), the HOH layer has linkage 2 (as in bafertisite-group minerals, where Ti(Nb) = 2 apfu): two Si_2O_7 groups of two H sheets link to two octahedra of the O sheet adjacent along b (Fig. 9c).

The chemical composition of the O sheet for both yoshimuraite and zinkgruvanite corresponds to the bafertisite-group minerals: only divalent cations (mostly Mn^{2+} and Fe^{2+}, respectively) are dominant in the O sheet (Sokolova and Cámara, 2017). However, the HOH layer with $Fe^{3+} = 2$ apfu has linkage 1, as in lamprophyllite-group minerals where Ti = 3 apfu, e.g. in barytolamprophyllite, ideally $(BaK)Ti_2Na_3Ti(Si_2O_7)_2O_2(OH)_2$, which has a completely different chemistry of the O sheet, i.e. Ti(Nb) and Na in the O sheet instead of 4 M^{2+} cations. Linkage and topology (as well as cell parameters) are very similar to those shown by innelite-1A (Sokolova et al., 2011) $Ba_4Ti_2Na_2M^{2+}Ti(Si_2O_7)_2[(SO_4)(PO_4)]O_2[O(OH)]$ (with M^{2+} = Mn, Fe^{2+}, Mg, Ca). But again, the chemical composition of the O sheet is very different, and so are site geometry and dimensions of polyhedra.

The difference in linkage between yoshimuraite and zinkgruvanite is to be ascribed to the different bond valence incident at the anions at the X^O_M sites coordinating cations at the M^H and M^O sites as discussed by Sokolova and Cámara (2014) (see their Fig. 2c). Longer M^H-X^O_M bonds occur when this M^H is occupied by Fe^{3+} (> 1.8 Å), therefore having a lower bond valence incident at X^O_M. Where Ti^{4+}(Nb^{5+}) occupies the M^H site, shorter M^H–X^O_M distances are observed (< 1.8 Å), providing bond valence excess. When linkage is of type 1, there is one octahedron in the O sheet having every apex shared with a polyhedron of the H sheet, which host high-charge cations. This implies that the cation at that octahedral site must be a low-charge cation and/or polyhedron size must grow (lamprophyllite-group minerals having Na at the O sheet) or the charge of the M^H site must be lower and the polyhedron must be larger (as in ericssonite-group minerals). Alternatively, a change in linkage that avoids having one octahedron in the O sheet sharing every apex with a polyhedron of the H sheet can keep a higher-charge cation, as in yoshimuraite.

This difference led Sokolova et al. (2018) to propose a separate group for ericssonite-group minerals (Fe^{3+} disilicates), which was approved by IMA (Memorandum 78-

Table 7. Selected interatomic distances (Å), polyhedral volumes and polyhedral distortion parameters for zinkgruvanite.

Si(1)	−O(3)	1.616(4)	*Si*(2)	−O(5)	1.614(4)	M^{H}	−O(3)	1.997(4)
	−O(12)	1.621(4)		−O(10)	1.640(4)		−O(5)	1.992(4)
	−O(10)	1.641(4)		−O(8)	1.617(4)		−O(4)	1.992(4)
	−O(4)	1.618(4)		−O(2)	1.609(4)		−O(9)	1.848(4)
< *Si*(1)	−O>	1.624	< *Si*(2)	−O(>	1.620		−O(2)	1.992(4)
V	(Å^3)	2.18	*V*	(Å^3)	2.166	< M^{H}	−O>	1.964
	TQE	1.0051		TQE	1.0051	*V*	(Å^3)	5.856
	TAV ($^{\circ 2}$)	20.76		TAV ($^{\circ 2}$)	20.50			
M(1)	−O(8) × 2	2.261(3)	*M*(2)	$-X^{O}_{A}$ × 2	2.272(11)	*M*(3)	−O(12) × 2	2.293(3)
	−O(12) × 2	2.258(3)		−O(8) × 2	2.119(4)		$-X^{O}_{A}$ × 2	2.077(11)
	−O(9) × 2	2.058(4)		−O(9) × 2	2.178(4)		−O(8)	2.250(3)
< *M*(1)	−O>	2.192	< *M*(2)	−O>	2.191	< *M*(3)	−O>	2.206
V	(Å^3)	13.59	*V*	(Å^3)	13.34	*V*	(Å^3)	13.75
	OQE	1.0241		OQE	1.035		OQE	1.030
	OAV ($^{\circ 2}$)	66.27		OAV ($^{\circ 2}$)	106.64		OAV ($^{\circ 2}$)	82.33
				$-X^{O}_{A(Cl)}$ × 2	2.518(12)		$-X^{O}_{A(Cl)}$ × 2	2.330(14)
S	−O(13)	1.435(5)	< *M*(2)	−O>	2.264	< *M*(3)	−O>	2.291
	−O(7)	1.483(4)	*V*	(Å^3)	15.18	*V*	(Å^3)	15.68
	−O(1)	1.485(5)		OQE	1.019		OQE	1.015
	−O(6)	1.479(4)		OAV ($^{\circ 2}$)	39.78		OAV ($^{\circ 2}$)	51.62
< *S*	−O>	1.471						
V	(Å^3)	1.626	A^{P}(1)	−O(10)	3.066(4)	B^{P}	−O(1)	2.951(5)
	TQE	1.0028		−O(5)	2.774(4)		−O(6)	2.895(5)
	TAV ($^{\circ 2}$)	11.35		−O(3)	2.830(4)		−O(5)	2.883(3)
				−O(6)	2.766(4)		−O(6)	2.858(4)
A^{P}(2)	−O(3)	2.700(3)		−O(2)	2.772(4)		−O(3)	2.887(3)
	−O(5)	2.570(3)		−O(1)	2.852(4)		−O(13)	2.675(5)
	−O(10)	2.780(3)		$-X^{O}_{A(Cl)}$	3.130(11)		−O(7)	2.858(4)
	−O(4)	2.650(3)		−O(4)	2.826(4)		−O(7)	2.888(5)
	−O(2)	2.530(3)		−O(10)	3.055(4)		−O(1)	2.963(5)
	−O(10)	2.870(3)		−O(7)	2.773(4)		−O(2)	2.870(3)
	$-X^{O}_{A(Cl)}$	2.520(5)	< A^{P}(1)	−O>	2.884		−O(4)	2.881(3)
< A^{P}(2)	−O>	2.660				< B^{P}	−O>	2.874
	$-X^{O}_{A(OH)}$	2.960(5)						
< A^{P}(2)	−O>	2.724	X^{O}_{A}	$-X^{O}_{A(OH)}$	0.446(15)			

* OQE: octahedral quadratic elongation. OAV: octahedral angle variance. TAV: tetrahedral angle variance. TQE: tetrahedral quadratic elongation in the sense of Robinson et al. (1971).

SM/17). Zinkgruvanite is a member of the ericssonite group (Sokolova et al., 2018), similar to ericssonite (Moore, 1971) and ferroericssonite (Kampf et al., 2011; Fig. 8), although it contains an interlayer of SO_4 that is absent in ericssonite. The discovery of this new species confirms the model of Sokolova and Cámara (2014).

Zinkgruvanite fits in the Strunz group 9.BE.25 (sorosilicates; Si_2O_7 groups, with additional anions; cations in octahedral and greater coordination; Strunz and Nickel, 2001).

7.1.4 Compositional variations

For the material investigated here, some chemical variation is present. The substitution of SiO_4^{4-} and PO_4^{3-} for SO_4^{2-} is coupled to variations in Ti^{4+} (Fig. 10). Heterovalent substitution of the oxyanion in the I block was also reported for yoshimuraite with $(P_{0.46}S_{0.34}Si_{0.17})_{\Sigma 0.97}O_4$ (McDonald et al., 2000). Some degree of heterovalent $Ti^{4+} \rightarrow Fe^{3+}$ substitution was reported by McDonald et al. (2000) in yoshimuraite. Since the $Ti^{4+} \rightarrow Fe^{3+}$ substitution affects the bond valence incident at cations of the O sheet and ultimately seems to control the topology of the crystal structure (linkage 1 in zinkgruvanite and linkage 2 in yoshimuraite), it seems reasonable to propose that at a certain $Ti^{4+} : Fe^{3+}$ ratio, the zinkgruvanite structure will transition to the yoshimuraite structure. In turn, the existence of intergrowths of yoshimuraite and zinkgruvanite seems possible and should be checked by transmission electron microscopy.

Table 8. Refined site scattering and assigned site populations for cation sites in zinkgruvanite.

Site	Refined site scattering (epfu)	Assigned site population (apfu)	Calculated site scat. (epfu)	$< M\text{-O} >_{obs.}$ (Å)	Ideal comp. (apfu)
$[5]M^H$	51.1(3)	$Fe^{3+}_{1.74} + Ti^{4+}_{0.20} + Al_{0.06}$	50.42	1.964	$2\ Fe^{3+}$
$[6]M(1)$	25.1(2)	$Mn^{2+}_{0.46} + Fe^{2+}_{0.41} + Fe^{3+}_{0.13}$	25.54	2.192	Mn^{2+}
$[6]M(2)$	47.94(8)	$Mn^{2+}_{0.87} + Fe^{2+}_{0.73} + Fe^{3+}_{0.29} + Mg_{0.11}$	49.59	2.191	Mn^{2+}
$[6]M(3)$	24.2(2)	$Mn^{2+}_{0.46} + Fe^{2+}_{0.42} + Ca_{0.10} + Ni_{0.01} + Zn_{0.01}$	25.00	2.206	Mn^{2+}
	97.24	$(Mn_{1.79}Fe^{2+}_{1.56}Fe^{3+}_{0.42}Mg_{0.11}Ca_{0.10}Ni_{0.01}Zn_{0.01})_{\Sigma 4.00}$	100.13		$4\ Mn^{2+}$
$[11]B^P$	55.4(2)	$Ba_{1.00}$	56.00	2.874	Ba
$[10]A^P(1)$	55.2(9)	$Ba_{0.97}$	53.35	2.884	Ba
$[7]A^P(2)$	0.9(1)	$Na_{0.03}$	0.33	2.660	□
	73.75	$(Ba_{1.97}Na_{0.03})_{\Sigma 2.00}$	73.30		Ba_2
$[4]S$	28.0(1)	$S_{1.62} + Si_{0.32} + P_{0.07}$	31.45	1.471	S_2

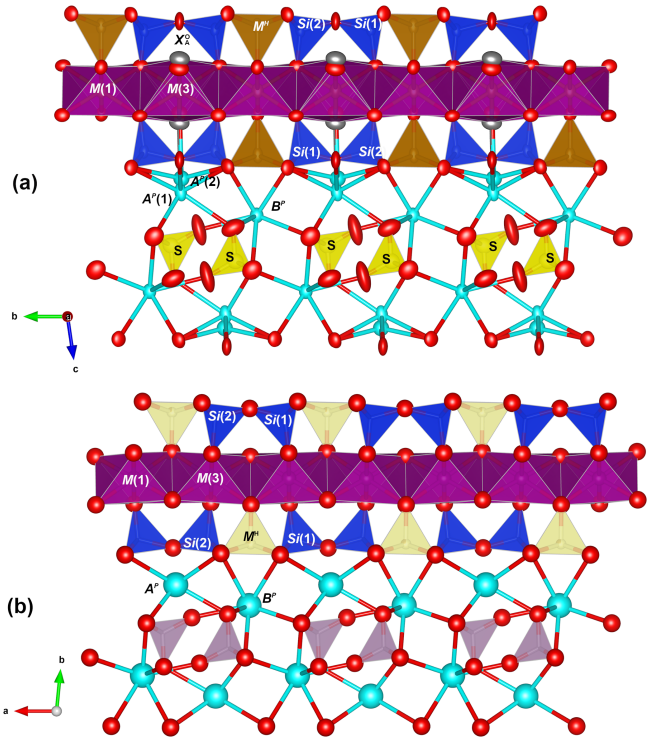

Figure 6. The crystal structures of zinkgruvanite **(a)** and yoshimuraite **(b)** (McDonald et al., 2000) for comparison. Mn^{2+} octahedra: purple; $Fe^{3+}O_5$ pyramid: light brown; $Ti^{4+}O_5$ pyramid: cyan; SiO_4 tetrahedra: blue; SO_4 tetrahedra: yellow; PO_4 tetrahedra: pink, Ba^{2+} cations: cyan; oxygen anions: red; chlorine anions: grey. Obtained with Vesta 3 (Momma and Izumi, 2011).

It is noteworthy that the homovalent $Mn^{2+} \rightarrow Fe^{2+}$ substitution is also significant in zinkgruvanite (but very limited for yoshimuraite; Watanabe et al., 1961; McDonald et al., 2000), and this suggests the possible occurrence of compositions with $Fe^{2+} \geq Mn^{2+}$ for zinkgruvanite (i.e. a "ferro-" analogue). As reported for yoshimuraite from the type locality (Watanabe et al., 1961), zinkgruvanite also shows the presence of some Cl, related to a $OH \rightarrow Cl$ substitution at the X^O_A site. The structural model of zinkgruvanite shows splitting of the ions at the X^O_A site, similar to what is observed for some Cl-bearing amphiboles (Oberti et al., 1993). This was not reported for ferroericssonite with 0.19 Cl atoms pfu (Kampf et al., 2011).

7.2 Genetic aspects

The minerals of the seidozerite supergroup commonly occur in highly differentiated magmatic complexes (peralkaline-to-agpaitic rocks). The type locality of the zinkgruvanite-related mineral yoshimuraite, the Noda-Tamagawa mine, is a metamorphosed bedded Mn deposit, in which the mineral occurs in the border facies of an alkaline pegmatite dike crosscutting the ores (Watanabe et al., 1961). Ericssonite-group minerals occur in skarn assemblages within metamor-

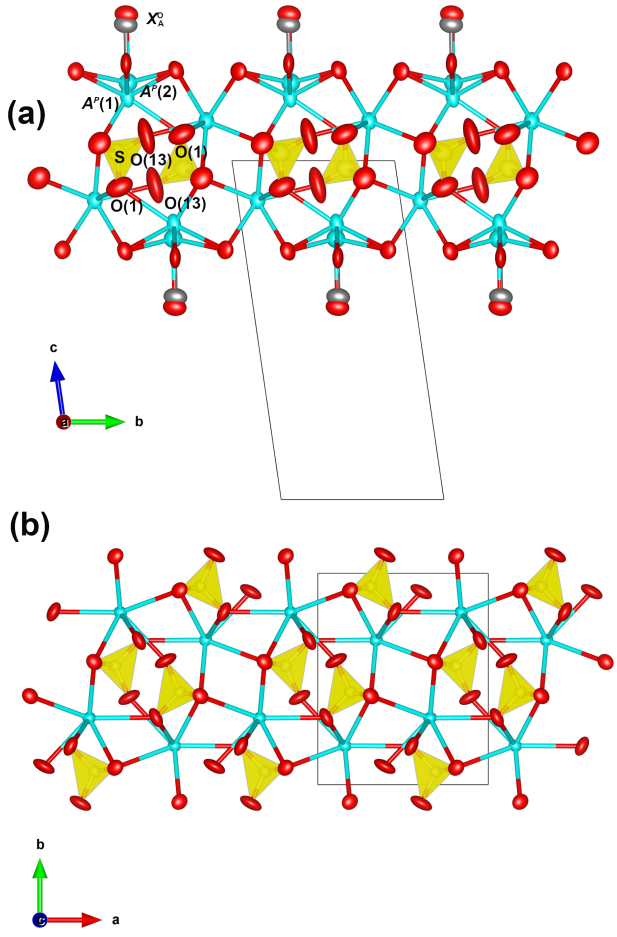

Figure 7. Comparison of the geometry of the intermediate block in zinkgruvanite **(a)** and a (010) slab of baryte **(b)**. Drawn with Vesta 3 (Momma and Izumi, 2011). Baryte model from Jacobsen et al. (1998).

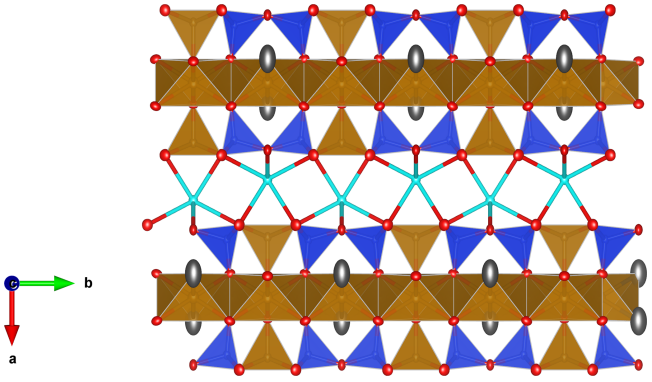

Figure 8. The crystal structure of ferroericssonite (Kampf et al., 2011) for comparison. Fe^{2+} octahedra: light brown; $Fe^{3+}O_5$ pyramid: light brown; SiO_4 tetrahedra: blue; Ba^{2+} cations: cyan; oxygen anions: red; chlorine anions and/or OH groups: grey. Drawn with Vesta 3 (Momma and Izumi, 2011).

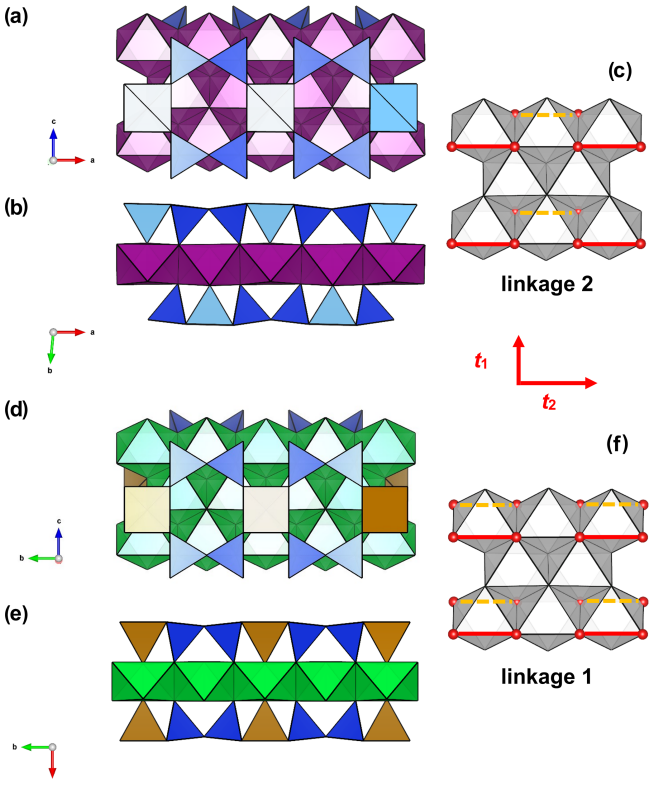

Figure 9. Linkage of H and O sheets in yoshimuraite: **(a)** the O (octahedral) sheet and the H (heteropolyhedral) sheet of (Si_2O_7) (in blue) and M^{H} polyhedra (in light yellow where occupied by Ti and in brown where occupied by Fe^{3+}) and **(b)** the TS block composed of HOH sheets; in zinkgruvanite **(d)** O + H sheets and **(e)** TS block composed of HOH sheets. M^{O} octahedra in purple centred by Mn and in green centred by Fe^{2+}. In yoshimuraite, linkage 2 occurs **(c)** where two Si_2O_7 groups link to two octahedra of the O sheet adjacent along t_2. In zinkgruvanite (ericssonite), linkage 1 occurs **(f)** where two H sheets connect to the O sheet such that two Si_2O_7 groups on opposite sides of the O sheet link to trans edges of the same octahedron of the O sheet.

phosed Mn ore deposits of inferred syngenetic origin (ericssonite; Moore, 1971; Matsubara and Nagashima, 1975) and in contact-metamorphosed Ba-rich sediments altered by late fluids (ferroericssonite; Dunning et al., 2018). Zinkgruvanite joins ericssonite through its occurrence in an originally syngenetic deposit which has been modified by regional metamorphism.

Geochemical studies by Hedström et al. (1989) and Jansson et al. (2017, 2018) demonstrated that all chemical components present in the Ba-rich associations were introduced already during the depositional stage of the stratiform Zn-Pb-Ag mineralization, via hydrothermal alteration of the stratigraphic footwall prior to regional metamorphism. Despite the rarity of the zinkgruvanite-bearing, Ba-rich associations at Zinkgruvan, they are not unusual with regards to the suite of elements, only with regards to the anomalously high Ba content and unusual mineralogy. It is suggested that these

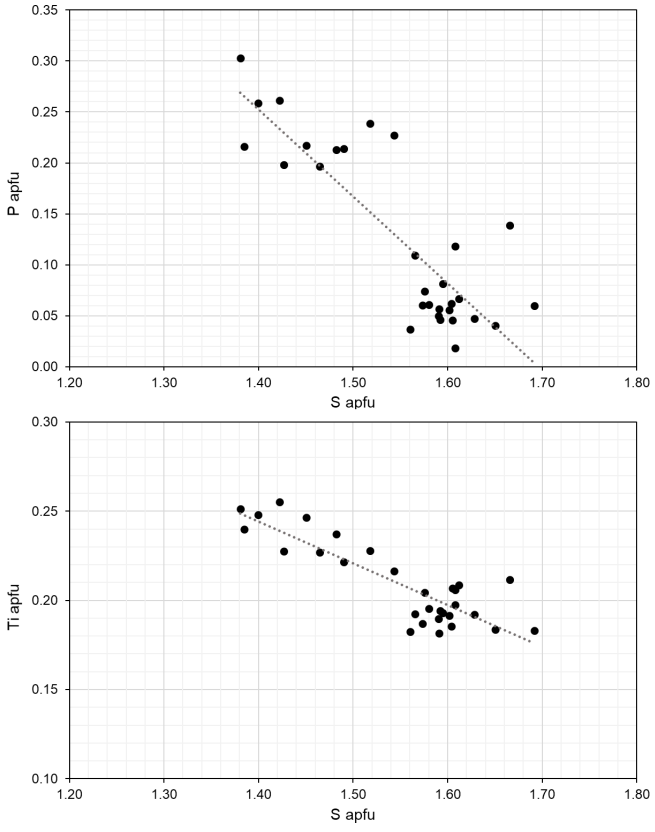

Figure 10. Compositional variations in zinkgruvanite based on EPMA. Regression lines correspond to $R^2 = 0.69$ and 0.74, respectively.

Ba-rich associations could have formed via internal remobilization and enrichment of syngenetic components during regional metamorphism or constitute a more unusual member of the pre-metamorphic alteration system, which formed the Zinkgruvan Zn-Pb-Ag deposit.

Jansson et al. (2017) interpreted that the stratiform Zn-Pb-Ag deposit and associated Cu mineralization formed upon exhalation of oxidized brines into a reducing seafloor environment. From the composition of zinkgruvanite and its associated minerals, it can be inferred that the fluids responsible for their formation were saline fluids enriched in Cl and F, as also indicated by the presence of minute grains of zhangpeishanite, BaFCl. The predominance of Fe^{3+} in zinkgruvanite and cerchiaraite contrasts with the stratiform Zn-Pb-Ag mineralization in general, which although being Fe-enriched is virtually devoid of Fe^{3+}. The great depth of the discovery location within the mineralization seem to preclude any influence of surficial oxidation, whereby alteration by oxidized brines is implicated.

The absolute timing of formation of zinkgruvanite and associated minerals such as barytocalcite, baryte, witherite and cerchiaraite is uncertain. The relatively coarse-grained, radial or generally diverging aggregates of mostly subhedral crystals in the form of a space-infill texture, seen in primarily barytocalcite and baryte (including interstitial infillings of cerchiaraite (s.l.)) between crystals, could be interpreted as vein- or fissure-filling assemblages formed by fluid-mediated processes. Somewhat speculatively, the formation of the exotic, Ba-Cl-F-enriched assemblage could have been connected to a late stage of devolatilization related to e.g. regional pressure release.

Data availability. A CIF file is deposited as the Supplement.

Supplement. The supplement related to this article is available online at: https://doi.org/10.5194/ejm-33-659-2021-supplement.

Author contributions. NJ found the mineral in a sample provided by AZ and made preliminary chemical analyses. AZ produced the graphical log core section. EJ, JL and AK made physical and optical observations. FC did the crystal structure solution and refinement. DH and AK obtained and interpreted spectroscopic data. JM performed EPMA work. DH coordinated the manuscript preparation, with substantial contributions from FC, NJ and EJ.

Competing interests. The contact author has declared that neither they nor their co-authors have any competing interests.

Disclaimer. Publisher's note: Copernicus Publications remains neutral with regard to jurisdictional claims in published maps and institutional affiliations.

Acknowledgements. The studied samples were collected during a research project in which Nils Jansson and Anders Zetterqvist participated and which was carried out as part of the strategic national innovation programme for the Swedish mining and metal-producing industry (STRIM) of Vinnova, Formas and the Swedish Energy Agency, with financial support from Zinkgruvan Mining AB, the Boliden Group and Lovisagruvan AB. Zinkgruvan Mining is thanked for granting permission to publish the results. Torbjörn Lorin is thanked for the colour photograph of zinkgruvanite in Fig. 2. Frank Hawthorne and Nikita V. Chukanov are thanked for useful suggestions. Fernando Cámara acknowledges financial support by the Ricerca Locale 2019 grant of the Università di Milano and from the Italian Ministry of Education, University and Research (MIUR) through the project "Dipartimenti di Eccellenza 2018–2022". Financial support for publication costs was generously given by Zinkgruvan AB.

Financial support. This research has been supported by the Italian Ministry of Education, University and Research (MIUR) and the Università di Milano (Dipartimenti di Eccellenza 2018–2022 and Ricerca Locale 2019).

Review statement. This paper was edited by Cristian Biagioni and reviewed by Frank Hawthorne and Nikita V. Chukanov.

References

Allen, R. L., Lundström, I., Ripa, M., and Christofferson, H.: Facies analysis of a 1.9 Ga, continental margin, back-arc, felsic caldera province with diverse Zn-Pb-Ag-(Cu-Au) sulfide and Fe oxide deposits, Bergslagen region, Sweden, Econ. Geol., 91, 979–1008, https://doi.org/10.2113/gsecongeo.91.6.979, 1996.

Andersson, U. B., Larsson, L., and Wikström, A.: Charnockites, pyroxene granulites, and garnet-cordierite gneisses at a boundary between Early Svecofennian rocks and Småland-Värmland granitoids, Karlskoga, southern Sweden, Geol. Fören. Stockh. För., 114, 1–15, https://doi.org/10.1080/11035899209453457, 1992.

Brown, I. D. and Altermatt, D.: Bond-valence parameters obtained from a systematic analysis of the Inorganic Crystal Structure Database, Acta Crystallogr., B41, 244–247, https://doi.org/10.1107/S0108768185002063, 1985.

Chukanov, N. V. and Chervonnyi, A. D.: Infrared spectroscopy of minerals and related compounds, Springer, Dordrecht, 1047 pp., 2016.

Dunning, G. E., Walstrom, R. E., and Lechner, W.: Barium silicate mineralogy of the western margin, North American Continent, Part 1: Geology, origin, paragenesis and mineral distribution from Baja California Norte, Mexico, western Canada and Alaska, USA, Baymin J., 19, 1–70, 2018.

Gagné, O. C. and Hawthorne, F. C.: Comprehensive derivation of bond-valence parameters for ion pairs involving oxygen, Acta Crystallogr., B71, 562–578, https://doi.org/10.1107/S2052520615016297, 2015.

Gunn, V. K.: Characterisation of the metamorphic, fluid and mineralisation history of the Zinkgruvan Zn-Pb-Ag deposit, Sweden, unpublished PhD thesis, University of Southampton, 275 pp., 2002.

Hålenius, U.: Mössbauer study of pentacoordinated ferric iron in orthoericssonite, Mineral. J., 17, 363–371, https://doi.org/10.2465/minerj.17.363, 1995.

Haugard, J.: En belgisk gruva vid norra Vättern, A-B, Seelig and C:o, Stockholm, 149 pp., 1944.

Hedström, P., Simeonov, A., and Malmström, L.: The Zinkgruvan ore deposit, south-central Sweden – a Proterozoic, proximal Zn-Pb-Ag deposit in distal volcanic facies, Econ. Geol., 84, 1235–1261, https://doi.org/10.2113/gsecongeo.84.5.1235, 1989.

Holtstam, D.: Jinshajiangite from the Norra Kärr alkaline intrusion, Jönköping, Sweden, GFF, 120, 373–374, https://doi.org/10.1080/11035899801204373, 1998.

Jacobsen, S. D., Smyth, J. R., Swope, R. J., and Downs, R. T.: Rigid-body character of the SO_4 groups in celestine, anglesite and barite, Can. Mineral., 36, 1053–1060, 1998.

Jansson, N. F., Zetterqvist, A., Allen, R. L., Billström, K., and Malmström, L.: Genesis of the Zinkgruvan stratiform Zn-Pb-Ag deposit and associated dolomite-hosted Cu ore, Bergslagen, Sweden, Ore Geol. Rev., 82, 285–308, https://doi.org/10.1016/j.oregeorev.2016.12.004, 2017.

Jansson, N. F., Zetterqvist, A., Allen, R. L., and Malmström, L.: Geochemical vectors for stratiform Zn-Pb-Ag sulfide and associated dolomite-hosted Cu mineralization at Zinkgruvan, Bergslagen, Sweden, J. Geochem. Explor., 190, 207–228, https://doi.org/10.1016/j.gexplo.2018.03.015, 2018.

Kampf, A. R., Roberts, A. C., Venance, K. E., Dunning, G. E., and Walstrom, R. E.: Ferroericssonite, the Fe^{2+} analogue of ericssonite, from Eastern Fresno County, California, USA, Can. Mineral., 49, 587–594, https://doi.org/10.3749/canmin.49.2.587, 2011.

Kampf, A. R., Roberts, A. C., Venance, K. E., Carbone, C., Belmonte, D., Dunning, G. E., and Walstrom, R. E.: Cerchiaraite-(Fe) and cerchiaraite-(Al), two new barium cyclosilicate chlorides from Italy and California, USA, Mineral. Mag., 77, 69–80, https://doi.org/10.1180/minmag.2013.077.1.07, 2013.

Mandarino, J. A.: The Gladstone-Dale relationship. IV. The compatibility concept and its application, Can. Mineral., 19, 441–450, 1981.

Matsubara, S. and Nagashima, K.: Orthoericssonite from the Hijikuzu mine, Iwate Prefecture, Japan, Mineral. J., 7, 513–525, https://doi.org/10.2465/minerj1953.7.513, 1975.

McDonald, A. M., Grice, J. D., and Chao, G. Y.: The crystal structure of yoshimuraite, a layered Ba-Mn-Ti silicophosphate, with comments of five-coordinated Ti^{4+}, Can. Mineral., 38, 649–656, https://doi.org/10.2113/gscanmin.38.3.649, 2000.

Momma, K. and Izumi, F.: VESTA 3 for three-dimensional visualization of crystal, volumetric and morphology data, J. Appl. Crystallogr., 44, 1272–1276, https://doi.org/10.1107/S0021889811038970, 2011.

Moore, P. B.: Ericssonite and orthoericssonite. Two new members of the lamprophyllite group, from Långban, Sweden, Lithos, 4, 137–145, https://doi.org/10.1016/0024-4937(71)90105-8, 1971.

Oberti, R., Ungaretti, L., Cannillo, E., and Hawthorne, F. C.: The mechanism of Cl incorporation in amphibole, Am. Mineral., 78, 746–752, 1993.

Pouchou, J. L. and Pichoir, F.: A new model for quantitative X-ray microanalysis. I. Application to the analysis of homogeneous samples, Réch. Aérospatiale, 3, 13–36, 1984.

Prescher, C., McCammon, C., and Dubrovinsky, L.: MossA: a program for analyzing energy-domain Mössbauer spectra from conventional and synchrotron sources, J. Appl. Crystallogr., 45, 329–331, https://doi.org/10.1107/S0021889812004979, 2012.

Robinson, K., Gibbs, G. V., and Ribbe, P. H.: Quadratic elongation: a quantitative measure of distortion in coordination polyhedra, Science, 172, 567–70, 1971.

Sheldrick, G. M.: Crystal Structure refinement with SHELX. Acta Crystallogr., C71, 3–8, https://doi.org/10.1107/S2053229614024218, 2015.

Sokolova, E.: From structure topology to chemical composition. I. Structural hierarchy and stereochemistry in titanium disilicate minerals, Can. Mineral., 44, 1273–1330, https://doi.org/10.2113/gscanmin.44.6.1273, 2006.

Sokolova, E. and Cámara, F.: From structure topology to chemical composition. XVII. Fe^{3+} versus Ti^{4+}: The topology of the HOH layer in ericssonite-2O, $Ba_2Fe_2^{3+}Mn_4(Si_2O_7)_2O_2(OH)_2$, ferroericssonite, $Ba_2Fe_2^{3+}Fe_4^{2+}(Si_2O_7)_2O_2(OH)_2$, and yoshimu-

raite, $Ba_4Ti_4^{+2}Mn_4(Si_2O_7)_2(PO_4)_2O_2(OH)_2$, Can. Mineral., 52, 569–576, https://doi.org/10.3749/canmin.52.3.569, 2014.

Sokolova, E. and Cámara, F.: The seidozerite supergroup of TS-block minerals: nomenclature and classification, with change of the following names: rinkite to rinkite-(Ce), mosandrite to mosandrite-(Ce), hainite to hainite-(Y) and innelite-1*T* to innelite-1*A*, Mineral. Mag., 81, 1457–1484, https://doi.org/10.1180/minmag.2017.081.010, 2017.

Sokolova, E., Abdu, Y., Hawthorne, F. C., Stepanov, A. V., Bekenova, G. K., and Kotel'nikov, P. E.: Cámaraite, $Ba_3NaTi_4(Fe^{2+},Mn)_8(Si_2O_7)_4O_4(OH, F)_7$. I. A new Ti-silicate mineral from the Verkhnee Espe Deposit, Akjailyautas Mountains, Kazakhstan, Mineral. Mag., 73, 847–854, https://doi.org/10.1180/minmag.2009.073.5.847, 2009.

Sokolova, E., Cámara, F., and Hawthorne, F .C.: From structure topology to chemical composition. XI. Titanium silicates: crystal structures of innelite-1*T* and innelite-2*M* from the Inagli massif, Yakutia, Russia, and the crystal chemistry of innelite, Mineral. Mag., 75, 2495–2518, https://doi.org/10.1180/minmag.2011.075.4.2495, 2011.

Sokolova, E., Hawthorne, F. C., Cámara, F., and Back, M. E.: The ericssonite group of Fe^{3+} disilicates minerals, Can. Mineral., 56, 95–99, https://doi.org/10.3749/canmin.1700064, 2018.

Stephens, M. B., Ripa, M., Lundström, I., Persson, L., Bergman, T., Ahl, M., Wahlgren, C. H., Persson, P. H., and Wickström, L.: Synthesis of the bedrock geology in the Bergslagen region, Fennoscandian Shield, south-central Sweden, Geological Survey of Sweden, BA58, 259 pp., 2009.

Stephens, M. B. and Jansson, N. F.: Paleoproterozoic (1.9–1.8 Ga) syn-orogenic magmatism, sedimentation and mineralization in the Bergslagen lithotectonic unit, Svecokarelian orogen, Geol. Soc. Mem., 50, 155–206, https://doi.org/10.1144/M50-2017-40, 2020.

Strunz, H. and Nickel, E.: Strunz Mineralogical Tables, Chemical-Structural Mineral Classification system, 9th Edn., E. Schweizerbart'sche Verlagsbuchhandlung, Stuttgart, Germany, 870 pp., 2001.

Tegengren, F.: Sveriges ädlare malmer och bergver, Sveriges geologiska undersökning Ca, 17, 654 pp., 1924.

Waldén, B.: Vieille Montagne, Hundra år i Sverige 1857–1957, AB Littorin Rydén Boktryckeri, Örebro, 236 pp., 1957.

Watanabe, T., Takéuchi, Y., and Ito, J.: The minerals of the Noda-Tamagawa mine, Iwate Prefecture, Japan. III. Yoshimuraite, a new barium-titanium-manganese silicate mineral, Mineral. Journ., 3, 156–167, https://doi.org/10.2465/minerj1953.3.156, 1961.

Wilson, A. J. C. (Ed.): International Tables for Crystallography, Volume C: Mathematical, physical and chemical tables, Kluwer Academic, Dordrecht, NL, 883 pp., 1992.

Young, B. B. and Millman, A. P.: Microhardness and deformation characteristics of ore minerals, T. I. Min. Metal., 73, 437–466, 1964.

Zhitova, E. S., Zolotarev, A. A., Krivovichev, S. V., Goncharov, A. G., Gabdrakhmanova, F. A., Vladykin, N. V., Krzhizhanovskaya, M. G., Shilovskikh, V. V., Vlasenko, N. S., and Zolotarev, A. A.: Temperature-induced iron oxidation in bafertisite $Ba_2Fe_4^{2+}Ti_2(Si_2O_7)_2O_2(OH)_2F_2$: X-ray diffraction and Mössbauer spectroscopy study, Hyperfine Interact., 238, 1–12, https://doi.org/10.1007/s10751-017-1468-9, 2017.